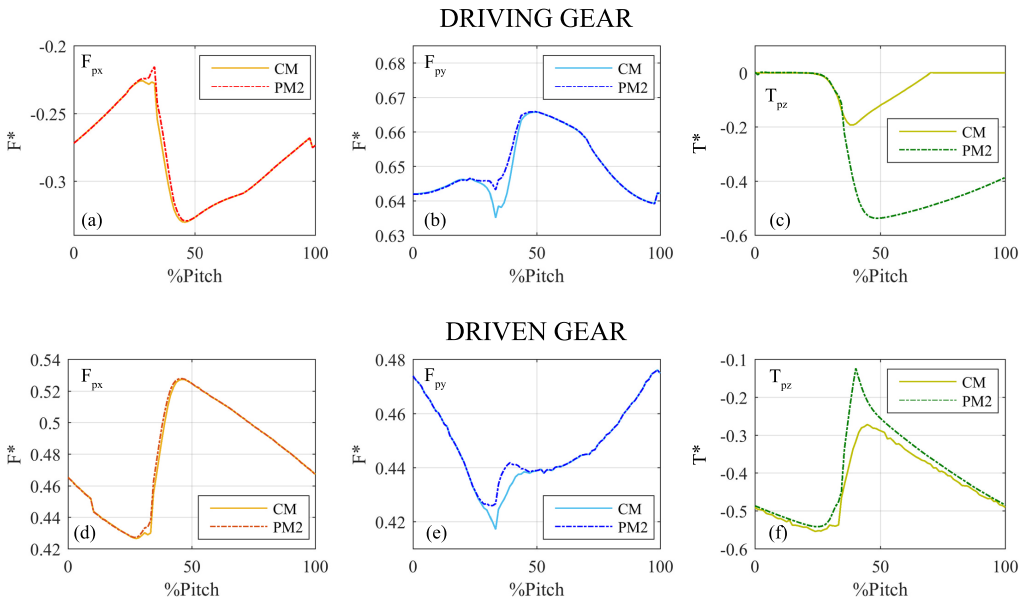

Figure 29: Comparison between pressure force and torque along the angular pitch for both driving and driven gear, calculated with the PM2 and the CM.

these results has to be found in the modeling procedure defined by PM2, in which the calculus is split in two sub-cases. When there are two pairs of teeth in contact (till about 40% of the angular pitch), the pressure torque estimation takes into account the oil pressure in the control volume between the two pairs of teeth. Therefore, within this angular interval, the pressure torque estimation is similar for both the PM2 and the CM and the results show a satisfactory agreement. When there is only a pair of teeth in contact, PM2 coincides with PM1, ergo the results show the same differences noticed in Figure 27.

Following this discussion, it can be affirmed that the estimation of the pressure force and torque transmitted by the oil to the gears is strongly influenced by the several phenomena that occur during the meshing interval. The omission of one of them affects the results with a relevance that depends on the angular extension of the neglected phenomenon itself.

3.5 PRESSURE FORCE AND TORQUE ESTIMATION IN CASE OF HELICAL GEARS

Hereinafter, the methodology described in Section 3.4 is extended to helical gears, with the aim to define a general method for pressure force and torque estimation. In order to estimate pressure force and torque under the effects of helix, the helical gear is sliced into an arbitrary number of cross sections, obtained by sectioning the helical gear along the face width direction. With this procedure, the cross sections appear as the lateral side of a spur gear and are equal each other, but with a different timing that depends on the helix angle. The methodology for calculating the pressure force and torque is applied to each cross section by using Eqns. 41-64, obtaining the evolution of such loads along a complete revolution. It has to be underlined that in case of helical gears the oil pressure is acting perpendicularly with respect to the teeth surface. Therefore, to correctly determine the pressure force components along axes x and y, pressures P_i, P_j and P_{j-1} should be multiplied by $\cos(\beta)$. Moreover, the application of the procedure from Eqn. 41 to Eqn. 64 to helical gears cannot be considered exhaustive: the particular shape of such gears necessarily causes the presence of non-zero components of the pressure force along the axial direction, and two more components of the pressure torque, along axes x and y. This aspect is clarified in the following Subsection 3.5.1, showing that the tooth spaces of a helical gear are loaded by the pressure torque even outside the meshing zone. Hence, it has to be considered that, in case of helical gears, pressure force and torque should be expressed along all the three Cartesian coordinates. Thus, with the aim of defining a general method, the procedure has been extended to all the remaining components.

The dissertation of the methodology is presented as follows: in Subsection 3.5.1 the pressure force and torque applied to helical tooth spaces outside the meshing zone are determined, later in Subsection 3.5.2 attention is focused on the calculation of the pressure loads applied to helical tooth spaces inside the meshing zone. The last subsection is devoted on analyzing pressure force and torque applied on the lateral sides of helical gears.

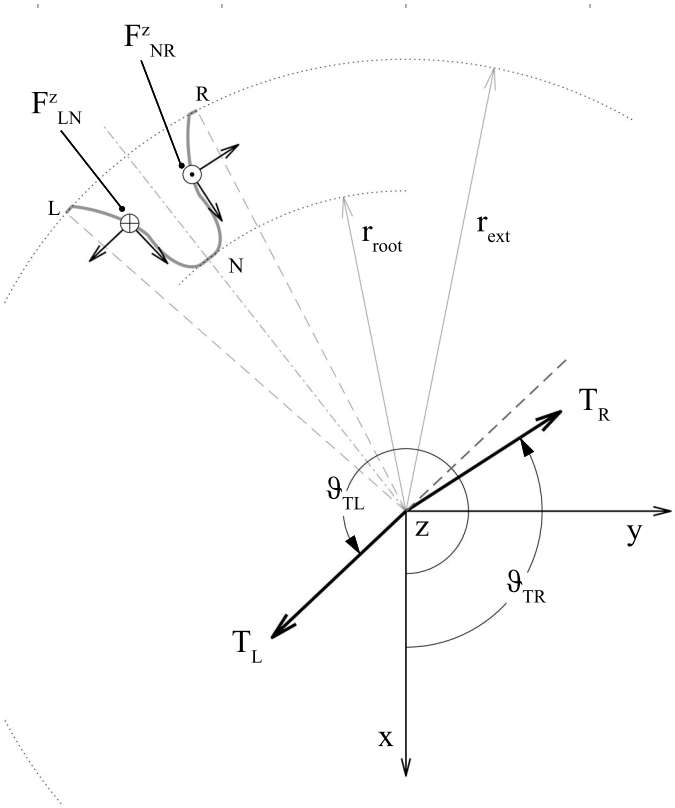

Figure 30: Pressure torque modeling in helical gears when the tooth space is outside the meshing zone.

3.5.1 *Helical tooth spaces out of the meshing zone*

Along the axial direction, the tooth space appears to be unbalanced only inside the meshing zone. Outside the meshing zone, since the tooth space is supposed to be loaded by a uniform pressure P_i, the axial component of the pressure force is zero, but, concurrently, two pressure torque components along axes x and y can be detected (as shown in Figure 30). For their estimation, an approach similar to the one proposed for the definition of the pressure torque along axial direction is hereinafter defined.

Focusing the attention on a tooth space outside the meshing zone, such a tooth space is not balanced with respect to the torque along axes x and y. Moreover, to calculate its value it is necessary to firstly divide the tooth space of each cross section in two symmetrical parts, namely right side and left

side, through its axial plane of symmetry and later determine the pressure force applied on each side along axis z. Thus, Eqn. 70 and 71 show the two opposite forces, which have the same amplitude and a different loading point (Figure 30).

$$F^z_{LN} = \pm \tan(\beta) \left(\frac{F_{LR,r}}{2} + P_i \cos(\beta)\, b\, (r_{ext} - r_{root}) \right) \tag{70}$$

$$F^z_{NR} = \mp \tan(\beta) \left(\frac{F_{LR,r}}{2} + P_i \cos(\beta)\, b\, (r_{ext} - r_{root}) \right) \tag{71}$$

The correct choice between plus or minus depends on the type of gears analyzed and, in particular, whether they are right handed or left handed gears. It is now possible to directly calculate the pressure torque along axis x and y using Eqns. 72 and 73.

$$T^z_{tot,i} = F^z_{NR} \frac{r_{ext} + r_{root}}{2} \cos\left(\vartheta_{T_R}\right) - F^z_{LN} \frac{r_{ext} + r_{root}}{2} \cos\left(\vartheta_{T_L}\right) \tag{72}$$

$$T^z_{tot,i} = F^z_{NR} \frac{r_{ext} + r_{root}}{2} \sin\left(\vartheta_{T_R}\right) - F^z_{LN} \frac{r_{ext} + r_{root}}{2} \sin\left(\vartheta_{T_L}\right) \tag{73}$$

By assuming that each force, F^z_{NR} and F^z_{LN}, acts along the axis of symmetry of the angular sector which defines it (as shown in Figure 30), angles ϑ_{T_R} and ϑ_{T_L} are defined by Eqns. 74 and 75 respectively:

$$\vartheta_{T_R} = \vartheta_R + \frac{2\pi}{4z_n} \mp \frac{\pi}{2} \tag{74}$$

$$\vartheta_{T_L} = \vartheta_L - \frac{2\pi}{4z_n} \pm \frac{\pi}{2} \tag{75}$$

where term $\frac{2\pi}{4z_n}$ represents a quarter of the angular pitch, while terms ϑ_R and ϑ_L are defined in Figure 24. Again, the correct choice between plus or minus depends on the type of gears analyzed.

3.5.2 *Helical tooth spaces into the meshing zone*

Inside the meshing zone, since the tooth pocket results to be loaded by different values of the oil pressure referring to the adopted discretization, the axial component of the pressure force is unbalanced. In this case, the calculus of the pressure force along the axial direction depends on the position of the contact point with respect to the line of action, as previously explained in Subsection 3.4.2 about the definition of F_{KH}. Within this framework, when the meshing occurs along the line of approach, force F^z_{KM} is equal to zero even if the radial component exists; the same effect is obtained regarding F^z_{MH} when the meshing occurs along the line of recess. Nevertheless, a single equation can be obtained to determine $F^z_{tot,i}$:

$$\begin{aligned} F^z_{tot,i} &= \pm \tan(\beta)\left(|F_{LK,r}| + |F_{LK,t}| - |F_{HR,r}| - |F_{HR,t}| + |F_{KM,t}| - |F_{MH,t}|\right) + \\ &\quad \pm \tan(\beta)\left(\frac{1 + sign(r_K - r_H)}{2}|F_{KM,r}|\right) + \\ &\quad \mp \tan(\beta)\left(\frac{1 - sign(r_K - r_H)}{2}|F_{MH,r}|\right) \end{aligned} \tag{76}$$

Again, the correct choice between plus or minus in Eqn. 76 depends on the type of gears analyzed.

The same procedure can be applied to tooth pockets inside the meshing zone. In particular, in Figures 25 and 26, the tooth pocket is divided into the two specular parts (right side causing T^{xy}_{HR}, T^{xy}_{NH}, and left side causing T^{xy}_{LK} and T^{xy}_{KN}) and their contribution to the pressure torque components along axes x and y is estimated. It has to be underlined that vector T^{xy} lies on the Cartesian plane defined by axes x and y in Figure 23. In particular, the pressure torque components caused by the left side are:

$$\left|T^{xy}_{LK}\right| = \tan(\beta)\left(|F_{LK,r}| + |F_{LK,t}|\right)\left(\frac{r_{ext} - r_K}{2}\right) \tag{77}$$

$$\begin{aligned} \left|T^{xy}_{KN}\right| &= \sin(\beta)\, bP_i 2r_K \sin\left(\frac{\vartheta_K - \vartheta_N}{2}\right)\left(\frac{r_{root} - r_K}{2}\right) + \\ &\quad + \sin(\beta)\, bP_i \left(\frac{r_K^2 - r_{root}^2}{2}\right) \end{aligned} \tag{78}$$

Concurrently, the pressure torque components caused by the right side are:

$$\left|T_{HR}^{xy}\right| = \tan(\beta)\left(|F_{HR,r}| + |F_{HR,t}|\right)\left(\frac{r_{ext} - r_K}{2}\right) \tag{79}$$

$$\begin{aligned}\left|T_{NH}^{xy}\right| &= \sin(\beta)\, bP_i 2r_H \sin\left(\frac{\vartheta_N - \vartheta_H}{2}\right)\left(\frac{r_{root} - r_H}{2}\right) + \\ &+ \sin(\beta)\, bP_i \left(\frac{r_H^2 - r_{root}^2}{2}\right)\end{aligned} \tag{80}$$

Therefore, the total pressure torque applied along the Cartesian axes x and y are obtained applying Eqns. 81 and 82, respectively:

$$\begin{aligned}T_{tot,i}^{x} &= \mp\left|T_{LK}^{xy}\right| \sin\left(\frac{\vartheta_L + \vartheta_K}{2}\right) \mp \left|T_{KN}^{xy}\right| \sin\left(\frac{\vartheta_K + \vartheta_N}{2}\right) + \\ &\pm\left|T_{NH}^{xy}\right| \sin\left(\frac{\vartheta_N + \vartheta_H}{2}\right) \pm \left|T_{HR}^{xy}\right| \sin\left(\frac{\vartheta_H + \vartheta_R}{2}\right)\end{aligned} \tag{81}$$

$$\begin{aligned}T_{tot,i}^{y} &= \pm\left|T_{LK}^{xy}\right| \cos\left(\frac{\vartheta_L + \vartheta_K}{2}\right) \pm \left|T_{KN}^{xy}\right| \cos\left(\frac{\vartheta_K + \vartheta_N}{2}\right) + \\ &\mp\left|T_{NH}^{xy}\right| \cos\left(\frac{\vartheta_N + \vartheta_H}{2}\right) \mp \left|T_{HR}^{xy}\right| \cos\left(\frac{\vartheta_H + \vartheta_R}{2}\right)\end{aligned} \tag{82}$$

Once the calculus (from Eqn. 41 to Eqn. 64 and then from Eqn. 70 to Eqn. 82) has been repeated for every cross section, which the helical gear was divided into, it is necessary to execute a numerical integration along the facewidth for all the components x, y and z of pressure force $F_{tot,i}$ and torque $T_{tot,i}$. The results are the pressure loads produced by the oil pressure inside a helical tooth space at a specific frame of calculus, i.e. a specific angular position. By repeating such a procedure at each angular position, it gives the pressure loads $F_{tot,i}$ and $T_{tot,i}$ along a complete revolution, for all Cartesian components. In order to obtain the total actions applied on the gear center along the angular pitch, Eqn. 65 must be applied and extended to every component of the pressure force and torque.

3.5.3 *Pressure load on the lateral sides of helical gears*

As debated in Subsection 3.4.3 regarding spur gears, the oil pressure on the lateral sides of helical gears may be taken into account for a general dissertation. Focusing the attention on a generic helical gear, it is clear that the two lateral sides appear as equal, but not symmetrical; in particular, since the two sides have the same shape, but a different timing, a specific pressure distribution on each gear side is detected. Moreover, it should be considered that the relative relief and grooves milled on the two sides of a common helical gear pump casing are not symmetrical; in particular, each of them is usually timed in reference to the lateral side of the gear which is facing to. For these reasons, even if the axial clearances are supposed as symmetrical, it is not possible to define a general procedure based on an analytical formulation, since several geometrical parameters referred to both the gears and the pump layout affect the pressure distribution on each gear side. Therefore, while in case of spur gears it is sometimes possible to estimate such loads following simple geometrical considerations, in case of helical gears numerical procedures appear to be compulsory, as proposed in [55]. Nevertheless, since the pressure loads defined on the two gear sides still tent to cancel each other out being applied on two opposite surfaces, the resulting pressure force and torque components are usually neglected in the analysis of the dynamic behavior of helical gear pumps [19].

3.5.4 *Evaluation of the methodology accuracy*

In the present section the results concerning the methodology presented in Subsections 3.5.1 and 3.5.2 are shown and discussed. As done in Subsection 3.4.4, in order to carry out the assessment, the pressure distribution referring to a gear pump with main parameters reported in Tab. 7 has been calculated by adopting the mathematical model described in Section 3.2. Since no other methods to calculate pressure force in helical gear pumps have been previously introduced in the literature, comparison with other estimation methodologies is not possible.

In Figure 31 the results regarding the pressure force (torque) provided by the application of the CM (Eqns. 41-64 and Eqns. 70-82) on the helical driving gear are shown as normalized by using Eqn. 68 and Eqn. 69. Focusing the

Table 7: Main characteristics of the pump adopted to assess the variable pressure loads estimation procedure.

Tooth number	11
Displacement	$2.6 * 10^{-4} m^3/rev$
Delivery pressure	$3bar$
Working speed	$3020rpm$

attention on the pressure force along the three axes, it can be noticed that F_{pz} has a considerable lower magnitude compared to F_{px} and F_{py}. The pressure force along the axial direction strongly depends on the helix angle, which is around 10° for the analyzed gears. Moreover, this aspect becomes even more effective by considering the pressure torque along axes x and y, which results to have a magnitude more than 100 times lower than along the axial direction. For this reason, the x and y components of the pressure torque could be neglected for the development of a simplified elasto-dynamic analysis of helical gear pumps. Nevertheless, they could become considerably high in case of high values of outlet pressure and important in order to study the pump balancing or its dynamic behavior.

3.6 MODEL IMPLEMENTATION AND WORKFLOW

The LP model presented in Sections 3.2, 3.3 and 3.4, which substantially constitutes the *processing* module of the whole model, has been entirely implemented in Matlab environment, together with the *pre-processing* one. The *post-processing* module, on the contrary, does not have a dedicated structure since the model outputs can be directly analyzed and post-processed by using built-in Matlab capabilities.

3.6.1 *Pre-processing module*

Despite the mathematical approach introduced in Section 3.2 may seem to require a small set of geometrical parameters referring to the analyzed gear pump, the pre-processing module represents the most time-consuming part of the entire model. With the aim to realize a stand alone model, i.e. a nu-

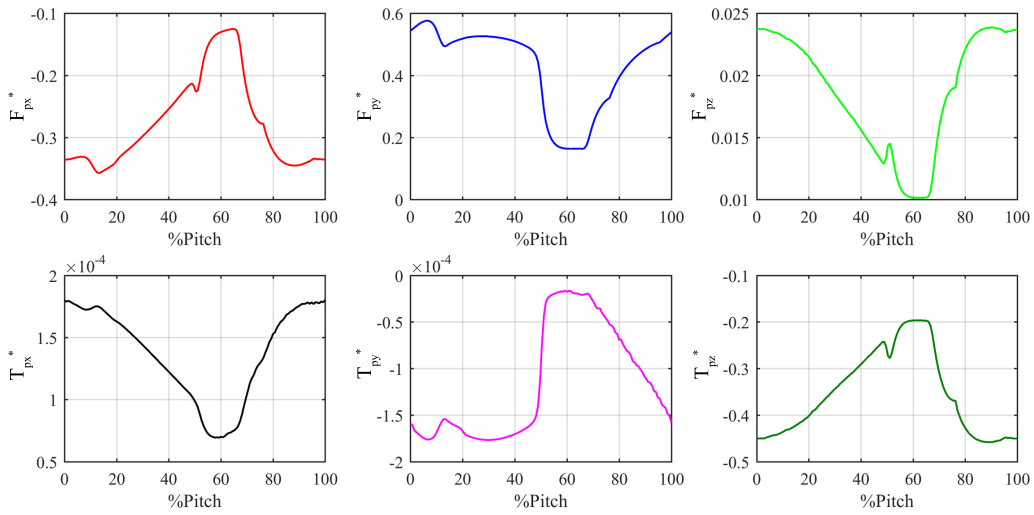

Figure 31: Pressure force and torque applied on the driving gear, in case of helical gear pumps.

merical model that does not need any external software except Matlab to run simulations, the pre-processing module includes the possibility to draw both the gearpair and an arbitrary number of grooves starting from the datasheet reporting the gear design parameters and the groove shape geometry parameters.

Once the starting data have been provided to the module, the software draws the gearpair by simulating the cutting process and it is consequently able to calculate (and store) independently all the geometrical data that are required by the processing module. In particular, as it can be appreciated from Eqns. 27, 29, 30 and 31, the evolution of several geometrical parameters, i.e. tooth pockets volume and its derivative, length, width and height of each flow channel, must be calculated along a complete revolution. Each parameter is calculated numerically, by using a dedicated function that simulates the meshing course throughout a revolution and determines the analyzed parameter at each frame of calculus.

If the analysis is focused on a spur gear pump, the pre-processing calculations are entirely performed in a 2D domain, by assuming no dependence from the axial direction. In order to clarify this aspect, it is possible to refer to the estimation of surface area A related to the cross section defining flow rate

Q_m^{ij-1} in Figure 16.b. Since no axial variations are taken into account, the evolution of surface area A along the meshing course is equivalent to the evolution of the minimum distance between the two tooth flanks, multiplied by the gear facewidth. The same approach is applied to all the parameters that physically extend themselves along the axial direction, such as gear pocket volumes. On the contrary, if the analysis is focused on a helical gear pump, influence of the helix is taken into account with a dedicated procedure. In particular, for all the geometrical parameters affected by a non-zero helix angle, both helical gears are sliced into an arbitrary number of cross sections, obtained by sectioning them along the face width. With this method, the cross sections are equal each other, but with a different timing. Let assume, for example, that the volume of a specific tooth pocket has to be calculated; firstly, for each defined cross section, the shape and the surface area of the tooth pocket are estimated along a complete revolution. Hence, a numerical integration is used to achieve the whole volume of the helical tooth pocket. To better underline the effects related to the application of this procedure, in Figure 32, volume V_i of a generic tooth pocket is firstly calculated by using the above-described procedure and then re-calculated without applying it, in order to obtain a spur gear. It is possible to observe that there are two main differences between them: (i) volume V_i is characterized by a wider meshing interval and, concurrently, (ii) it shows smoother variations, which are two typical features provided by helical gears. Such a procedure is similarly applied to all the parameters affected by the presence of the helical.

Once the entire set of parameters has been obtained for both gears, look-up tables are generated and stored by timing the data with respect to the starting reference position of the gearpair. This last step produces all the required geometrical data to run the dynamic simulations. Therefore, at the very first run of the code, all the geometrical parameters need to be calculated and the pre-processing step may require a considerable amount of time; however, when this step is concluded, it is possible to simulate whatever working condition without repeating it. Moreover, since the pre-processing module is made by a number of separated sub-modules, each one referring to the calculation of a specific geometrical parameter, design modifications may be introduced and analyzed without necessarily run the entire module. Let assume, for example, that a different relief groove shape wants to be investigated. Since the gearpair is not affected by the design modification, it is not necessary to re-calculate

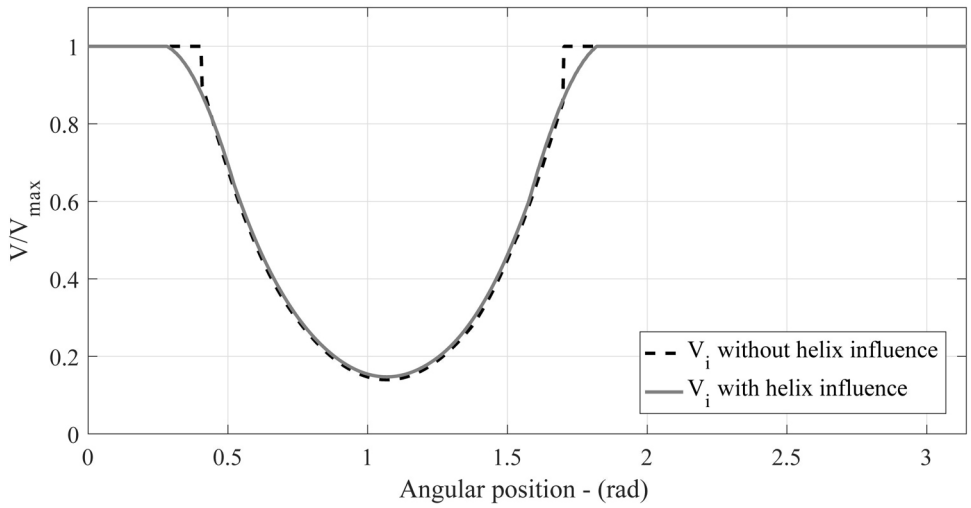

Figure 32: Comparison between V_i calculated as belonging to a spur gear and V_i calculated with the specific procedure for helical gears (V_{max} is the maximum value of volume V_i).

pocket volumes nor the surface areas referred to flow rates Q_m^i, Q_m^{ij-1}, Q_{outlet}^i and Q_{inlet}^i in Figure 16, obtaining so the positive effect to reduce the computational effort requested.

3.6.2 *Processing module*

The processing module allows to set the pump working conditions and to numerically solve the dynamic system defined in Section 3.2 with respect to the gearpair translational micromotions, that are calculated by using the approach proposed in Section 3.3.

Before starting each simulation, the code requires to define the boundary conditions, i.e. mean inlet/outlet pressure, as well as the initial conditions, i.e. the pressure field at initial time $t = 0$. Moreover, on the basis of the approach proposed in Section 3.3, if the gearpair has $\tau = 1$, then the driving torque must be provided, in order to calculate mesh force F_m from Eqn. 36. It is worth noting that the other parameters required by Eqn. 36, i.e. pressure torque $T_p^{(1)}$ and $T_p^{(2)}$, are automatically calculated by the code from the initial condition referred to the pressure field. On the other hand, in the case where

$\tau \neq 1$, then F_m is obtained from Eqn. 39 and therefore both driving torque T_{shaft} and hydro-mechanical efficiency η_{HM} must be defined. Such data may be, in general, obtained from direct measurements [78] or, in case no prototypes are available, by estimating them with specific models [79, 37]. Finally, last requested parameters refer to the working speed ω and the oil physical properties, i.e. bulk modulus B, dynamic viscosity μ and density ρ.

Once boundary and initial conditions, together with working condition parameters, have been defined, the module is effectively ready to solve the dynamic system. As already introduced in Section 3.1, the pressure field is estimated in reference to the gearpair micromotions, that are actually predicted by taking into account the variable pressure loads produced by the pressure field and the bearing reaction. In order to better understand how the iterative solution scheme does work, it is possible to focus the attention on the chart in Figure 33, which describes the solution workflow for a generic angular position of the gearpair. At the first iteration, the code uses the solution of the previous angular position as starting data to get the first estimation of the gear centers position, which is achieved by using Matlab function *fsolve* applied to Eqn. 34. By knowing the gearpair translational motion, the code then updates all the influenced geometrical parameters and collects the new look-up tables. In particular, the process of parameter updating is applied to the main pump radial clearances, i.e. tooth tip clearances, bearing radial clearances and backlash value, while all the axial parameters are considered as constant values. It is worth underlining that also the pocket volume depends on the gearpair micromotions, however, such a relation is neglected in the proposed model. The reason behind this assumption is justified by the fact that the bearing radial clearance is so small that its influence on the pocket volume estimation is less than the 0.1% of the volume nominal value and it is therefore not appreciable on the model results. Once all the position dependent data have been recalculated, the dynamic system is solved by taking the solution of the previous angular position as initial condition. Since the overall fluid-dynamic system based on Eqn. 29 is typically stiff, variable-stepsize variable-order Matlab function *ode15s* is used to obtain the solution. Finally, pressure force and torque are calculated on the basis of the new pressure field estimation. Since at the end of the first iteration no comparable terms are available, the code directly goes for the second turn, by using the pressure field just calculated to obtain a new gearpair centers position. Once the calculus is entirely repeated

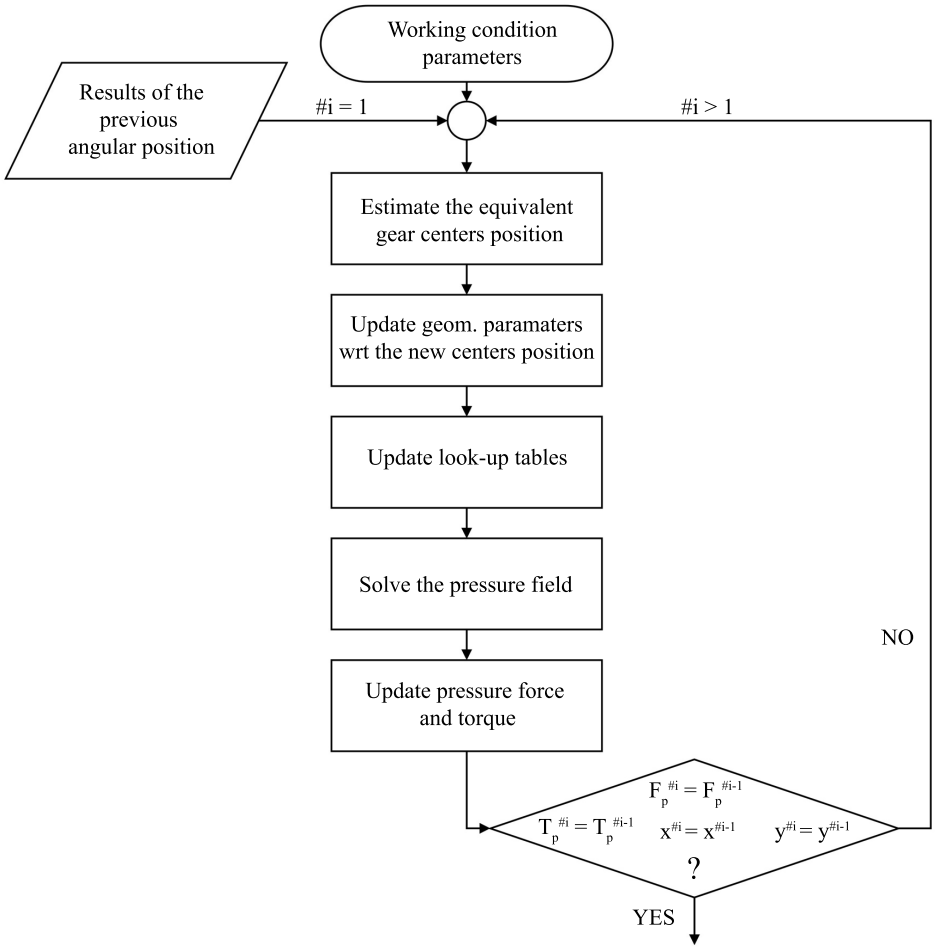

Figure 33: Iterative solution scheme for a given gearpair angular position, where #i stands for iteration number.

for the second time, then pressure force, torque and centers position estimated by two consecutive iterations are compared; if the relative tolerance of each term is under the threshold value, then solution set from the last iteration is stored and the code moves to the next angular position. Otherwise, in case at least one term shows a relative tolerance above the threshold value, then the code moves to another iteration referred to the same angular position. The procedure is repeated until the tolerance condition is satisfied or the iteration number reaches a limit value.

The convergence of the calculus is usually pretty fast and three-four iterations are sufficient to satisfy a tolerance condition with a threshold value equal to 10^{-3}. However, on the basis of the author's experience, the maximum number of iterations should always be fixed, since in case of low speed or light loads, the code might tend to fall in a local minimum.

3.7 EXPERIMENTAL CAMPAIGN

The validation of the presented model has been achieved by means of a dedicated experimental campaign. The test rig adopted to carry out the tests is shown in Figure 34. The gear pump is installed inside a sealing box that makes it working submerged and driven by a brushless AC motor with speed controller; a torque meter is located along the shaft connecting the pump with the electric motor. The pipeline for the oil supply system is constituted by two branches: one connecting the tank to the sealing box and the other one connecting the pump's outlet chamber to the tank. An automatic servo valve located on the latter branch of the pipeline allows for the fast regulation of the oil delivery pressure. The oil temperature is regulated with an additional pipeline connected to the tank and controlled by a dedicated system, namely the temperature controller. Such a system monitors the oil inside the tank by using a thermocouple and regulates the temperature with a number of electric resistances. Both pipeline systems described above are equipped with a drainage system, various valves and filters in order to allow for a safe and easy management of the test rig during the measurement procedures. The description of such auxiliary parts of the test rig is neglected being out of the scope of the present work. As shown in Figure 34, the set of transducers adopted for the tests is constituted by two digital pressure gauges placed on the suction and delivery ports, respectively, and a Kracht Gear Type Flow Meter, placed on the delivery pipeline, in order to measure the outlet flow rate and therefore determine the volumetric efficiency. The instantaneous angular speed can be directly acquired from the tachometer connected to the speed controller of the electric motor. The set of sensors is acquired by the data acquisition system integrated in the test bench.

In order to carry out the experiments, an external gear pump has been designed and manufactured; the main design parameters are reported in Table 8. As it can be noted, the gearpair is constituted by two helical gears with

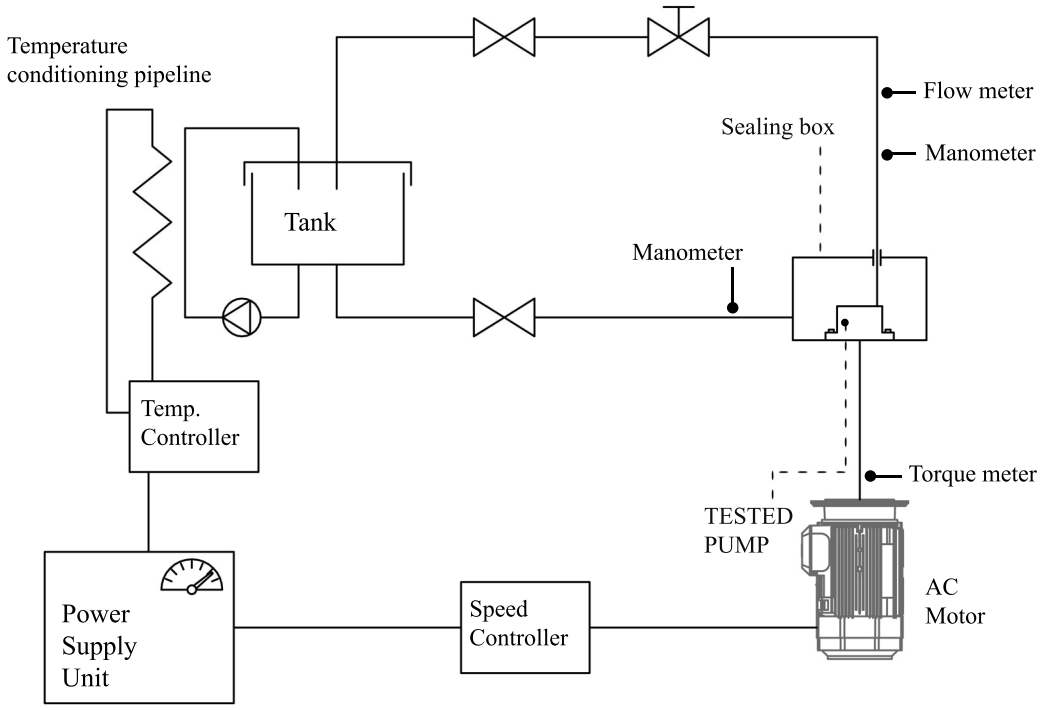

Figure 34: Test rig configuration and sensors disposition adopted for the experimental campaign.

different tooth number, so that $\tau \neq 1$; despite this choice might be considered unusual, studies as the one reported in [41] are making it more and more common. Figure 35 shows the mechanical setup of the pump; the helical gearpair is located inside a cast iron casing, therefore radial clearances on both driving and driven side are designed to not require any running in process, since contact friction between tooth tips and casing cannot take place. Gears are then covered by a thrustplate and the entire machine is packed by a coverplate, which is clumped to the casing with four screws. A rubber seal is placed between the casing and the coverplate, in order to reduce leakage. Journal bearings are directly obtained from the casing and the coverplate, while grooves are milled on the thrustplate and the casing. The pump is designed to work in submerged conditions, as usually required for pumps working as oil supplier in automatic transmissions.

Table 8: Main design parameters of the designed gear pump.

Tooth geometry	helical
z_1	14
z_2	9
Displacement Vm	$14.65 cm^3/rev$
Facewidth b	$26 mm$
Normal module m_n	$2.25 mm$
Helix angle β	$6 deg$

The designed pump has been manufactured in 20 nominally identical samples, in order to perform a statistical characterization of the pump behavior. As a matter of fact, despite each sample is based on the same design that should lead to 20 identical pumps, design tolerances, together with the accuracy of the production process, necessarily cause the presence of minor discrepancies. As a result, the 20 samples will globally show the same macro-behavior; however, each pump will also have its own characteristic curve. It is therefore clear that, to proper address the accuracy of the proposed model, first a detailed characterization of the samples is mandatory. On the basis of this consideration, the mean actual value of the tooth-tip/casing clearances and bearing radial clearances has been measured on both gears for each pump, at the end of the production process. Grooves milled inside the pressurizing zones of the gearpair have not been included in this study since they are obtained with very small design tolerances. Moreover, measurements on the actual axial clearances have not been taken into account, since axial leakages are assumed to be of secondary importance with respect to radial leakages. This assumption is made on the practical basis that the tooth tips, which are responsible for radial leakages, are particularly thin in both gears with respect to the mean tooth width, which is responsible for axial leakages. Moreover, the pump has been designed with mean radial clearance values that are almost the double of the mean axial clearance values.

Charts in Figures 36.a and 37.a report the measured tooth tip and journal bearing radial clearances (for both gears), respectively. For confidentiality rea-

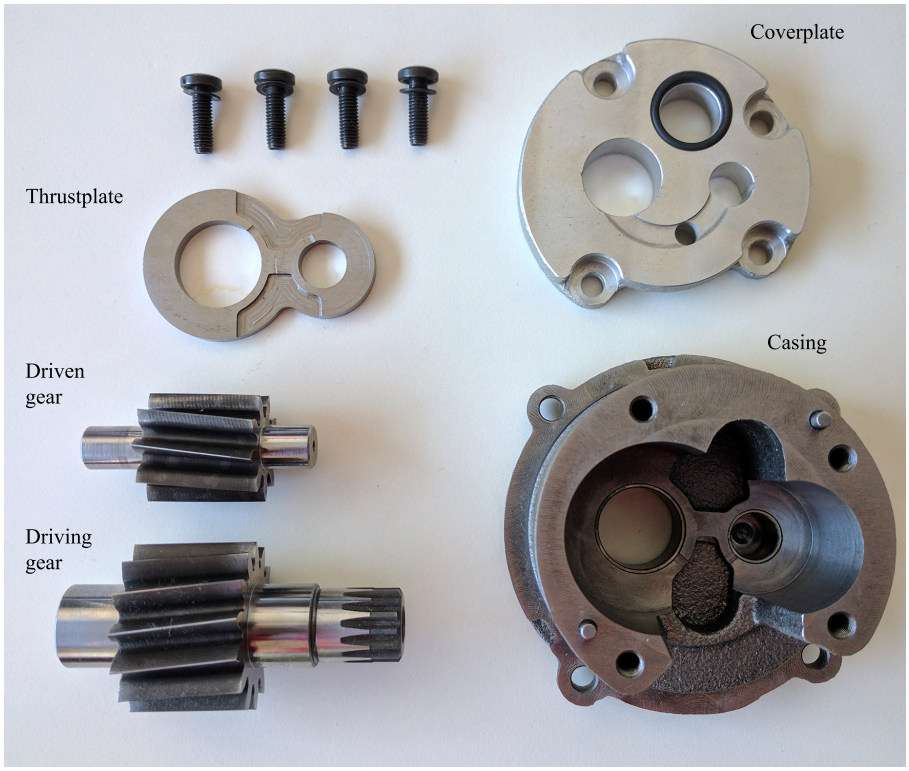

Figure 35: Mechanical setup of the tested pump.

sons, measured data x_m have been normalized with respect to the reference design value x_d as shown in Eqn. 83:

$$x_m^* = \frac{x_m - x_d}{x_d} \tag{83}$$

As it can be noted, both tooth tip/case and journal bearing clearances may deviate consistently from the design value. In particular, for tooth tip radial clearances (Figure 36), the mean deviation of the measured data from the design value is around 2.5% for the driving gear (Figure 36.b) and 3.5% for the driven one (Figure 36.c); moreover, such a deviation may occasionally reach also the 20%, leading to a standard deviation around 6% for both gears. A similar situation, but amplified, is observed in the case of journal bearing radial clearances: the mean deviation of the measured data is around -10% for the driving gear (Figure 37.b) and reaches almost the 17% for the driven one (Figure 37.c). Standard deviation in both gears is similar to the one observed

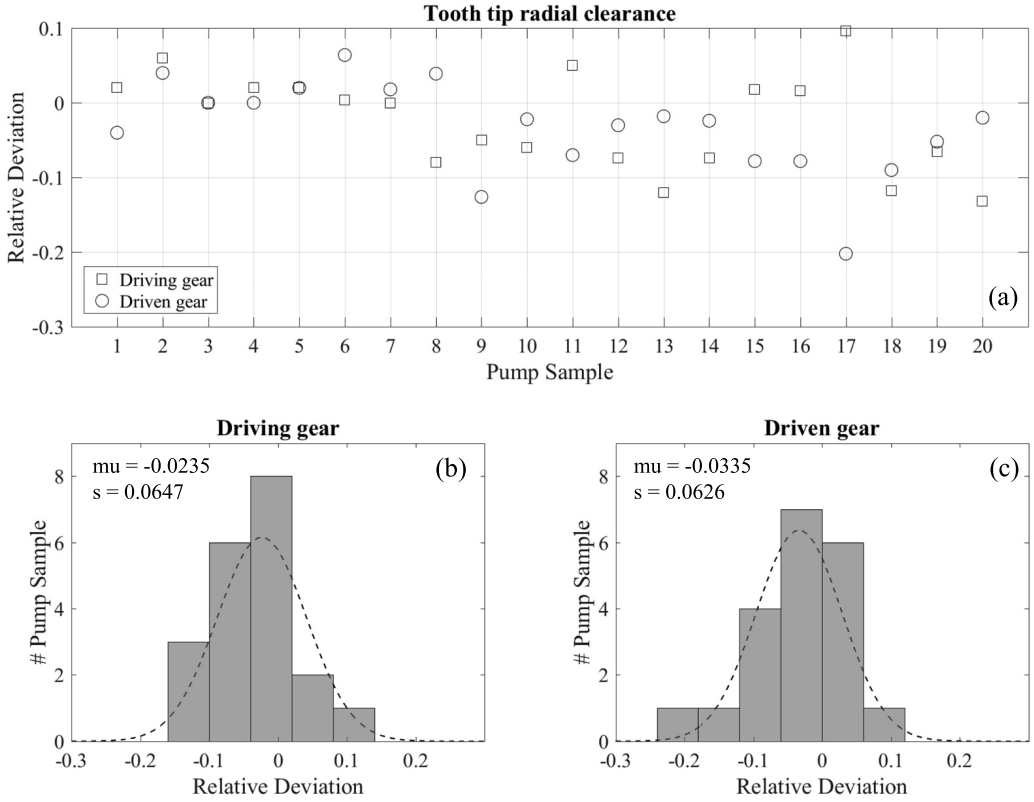

Figure 36: Measured tooth tip clearances deviation from the design value. Dash line represents the normal distribution with estimated parameters mu and s.

in case of tooth tip clearances. Normality of the measured data has been previously verified by means of a chi-squared normality test. The results of this analysis demonstrate that actual clearances may deviate consistently (but still within the design tolerances of some micrometers) from the design values, suggesting that this aspect should be taken into account in the validation of the model. However, in order to evaluate their actual effect on the pump behavior, attention must be focused also on the measured pump performance.

With the aim to characterize the pump throughout a wide working conditions range, two different tests have been conducted. The first testing procedure consists in evaluating the pump performances at four different operating speed values, while delivery pressure is kept as a constant. On the contrary,

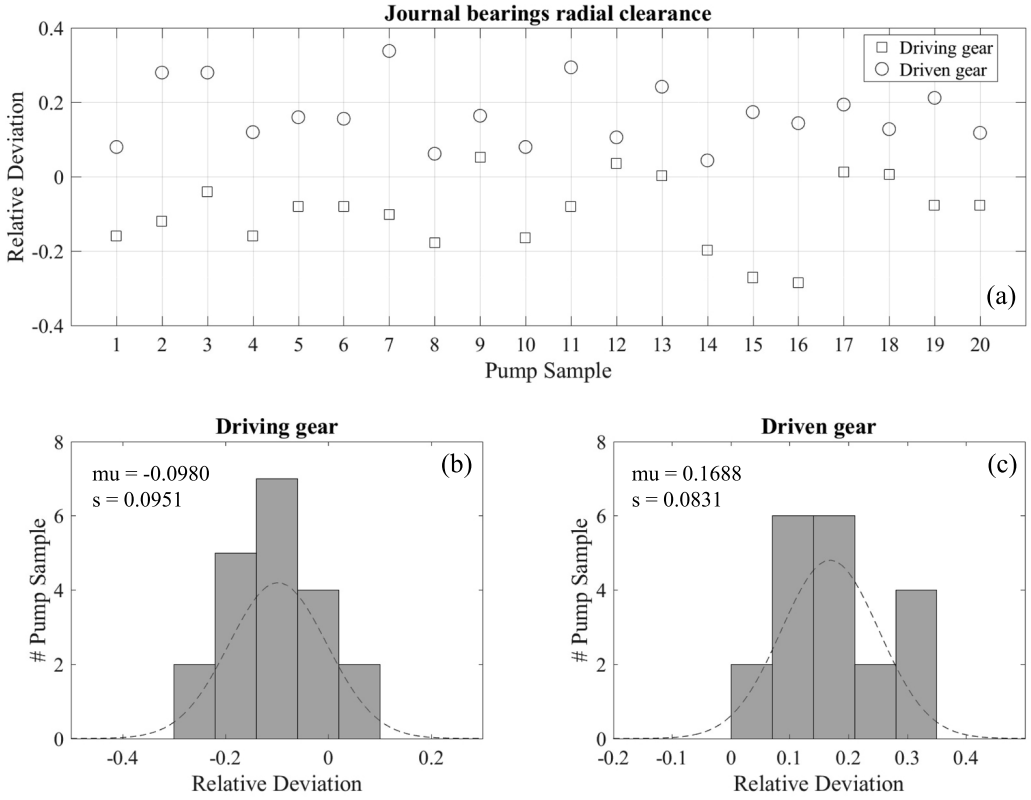

Figure 37: Measured journal bearing clearances deviation from the design value. Dash line represents the normal distribution with estimated parameters mu and s.

the second testing procedure consists in evaluating the pump performances at different delivery pressure values, while the working speed is kept as a constant. Both testing procedures have been repeated at two different oil temperatures. Table 9 summarizes the sixteen working conditions tested; the entire set of tests has been repeated for each pump sample, leading to 320 different tests.

Figure 38, from (a) to (e), shows the measured volumetric efficiency values with respect to delivery pressure variation for the entire set of 20 samples; data have been collected at a working speed equal to 1000rpm and oil temperature equal to 60°C. Efficiency is estimated by dividing the measured

Table 9: Test conditions adopted for the experimental campaign.

Outlet pressure (bar)	Oil temperature (°C)	Working speed (rpm)
30	60	500
		1000
		2000
		4000
	120	500
		1000
		2000
		4000
10	60	1000
20		
30		
40		
10	120	
20		
30		
40		

delivery flowrate by its theoretical value, which is defined by the pump displacement Vm in Tab. 8 and the mean working speed (see Ref. [80]). As it can be appreciated from Figure 38.a, efficiency tends to decrease as the delivery pressure increases, as expected by a fixed displacement pump. For constant values of the working speed and the oil temperature, pressure dependent hydraulic losses, i.e. leakage flowrates, tend to increase monotonically as also explained in Ref. [80], p. 87. Figure 38 also demonstrates that volumetric efficiency decreases as the oil temperature is increased. Such a behavior is due to the decrease observed in the oil dynamic viscosity as a consequence of the positive variation of the temperature, since part of the volumetric losses is inversely proportional to the fluid viscosity itself. It is worth specifying that the viscosity decrease concurrently causes a decrease of the pressure drop at the

inlet port, which would have the beneficial effect of increasing the delivered flowrate (see Ref. [80], p. 87). However, the latter effect becomes predominant only above a limit value of the oil viscosity, which is usually too high to be reached for the considered application. What is more interesting relates to how the measured values are distributed: in particular, it can be noted that, as the delivery pressure increases, the standard deviation tends to increase as well. A similar trend is also appreciated in Figure 38 from (f) to (l), which shows the measured efficiency values with respect to delivery pressure variation, collected at a working speed equal to $1000\mathrm{rpm}$ and oil temperature equal to 120°C. In both cases, the increment of the standard deviation between two consecutive pressure conditions is almost a constant; moreover, such a increment is almost equal by comparing tests at 60°C with tests at 120°C. However, estimated standard deviations differ consistently in their absolute value between the two test conditions. In order to better enlighten this aspect, it is possible to focus the attention on Figures 38.b and 38.e, which report the histogram of measured efficiency values at $P_{out} = 10\mathrm{bar}$ and $P_{out} = 40\mathrm{bar}$ at $T_{oil} = 60°C$, respectively. As it can be noticed, standard deviation changes from $s = 0.0115$ to $s = 0.0299$ by showing an increment around 0.019. Concurrently, by focusing the attention on Figures 38.g and 38.l, which report the histogram of measured efficiency values at $P_{out} = 10\mathrm{bar}$ and $P_{out} = 40\mathrm{bar}$ at $T_{oil} = 120°C$, it results that standard deviation changes from $s = 0.0217$ to $s = 0.0399$ and therefore it shows almost the same increment of the previous case. Nevertheless, by comparing measured data at the same delivery pressure but with a different oil temperature, e.g. Figures 38.b and 38.g, it is noted that the temperature increasing causes both a reduction of the mean volumetric efficiency and an increase of the standard deviation.

Measured data referring to volumetric efficiency with respect to speed variation have been post-processed with the same approach (see Figure 39). In particular, from Figure 39.a to 39.e, measured efficiency values for the 20 samples at a delivery pressure $P_{out} = 30\mathrm{bar}$ and $T_{oil} = 60°C$ are shown together with the estimated mean value and standard deviation for the four different working speed analyzed. As it can be appreciated, the speed increasing causes the volumetric efficiency to slightly increase as well (in agreement with Ref. [80], p. 87), while the standard deviation tends to decrease. This behavior is qualitatively the opposite if compared to the pressure increasing; moreover, such a trend is confirmed also for an oil temperature equal to 120°C. As al-

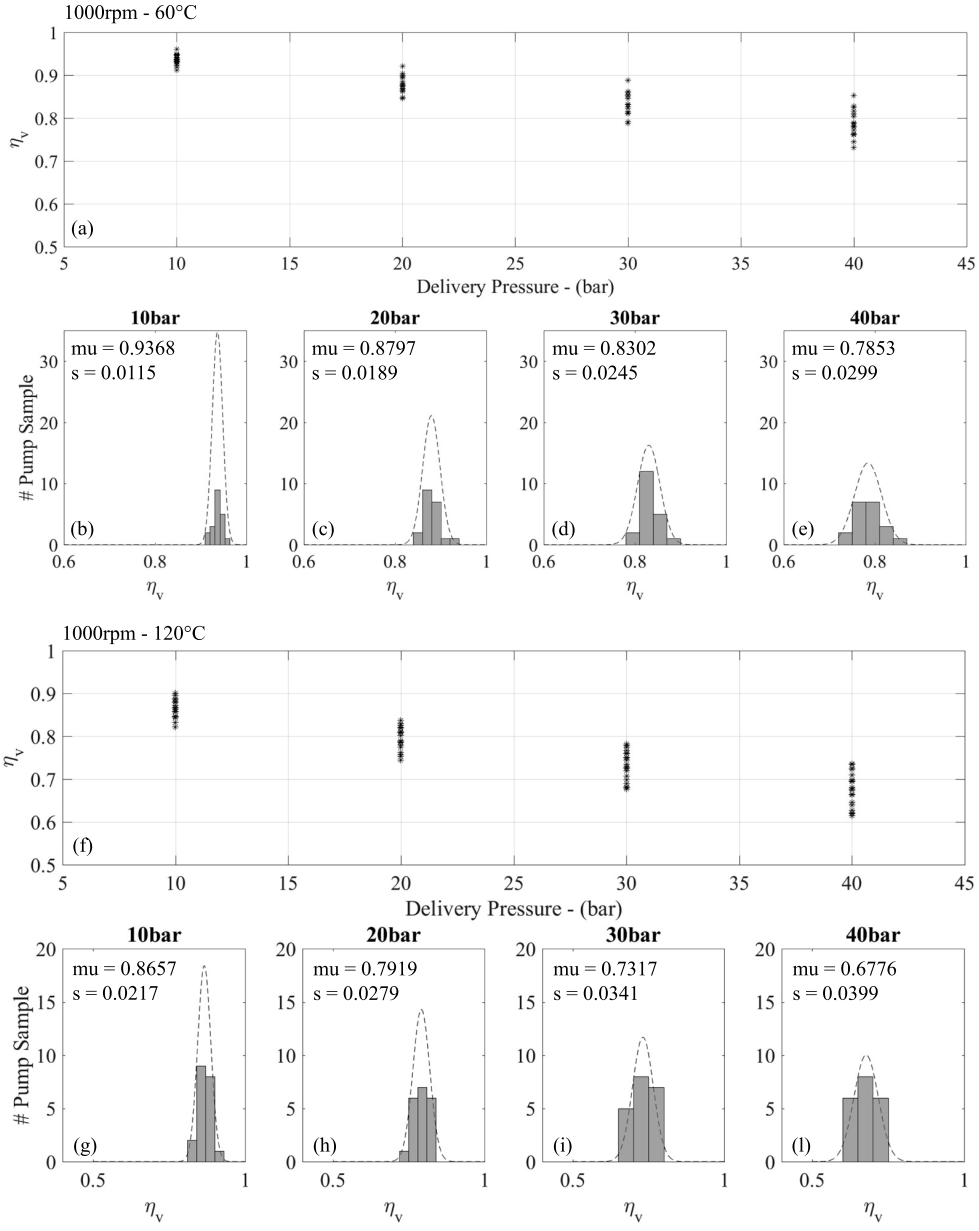

Figure 38: Measured efficiency η_v with respect to pressure variation, for the 20 samples. From (a) to (e), test conditions are: $n = 1000rpm$ and $T_{oil} = 60°C$, while from (f) to (l) test conditions are: $n = 1000rpm$ and $Temp = 120°C$. Data are normally distributed for each analyzed working condition.

ready observed when evaluating measured efficiency with respect to delivery pressure variations, for a given working condition, the oil temperature causes also the standard deviation to increase. However, in this case the standard deviation increment produced by the oil temperature increase is much less evident.

Similar behavior has been also observed in the measured torque required to operate the pump, as it can be appreciated from Figure 40 depicting the required torque with respect to delivery pressure and Figure 41 depicting the required torque with respect to working speed (torque and efficiency data have been recorded simultaneously, during the same test). In agreement to the previous considerations, the temperature increase tends to spread the measured data, as demonstrated by the increment observed in the standard deviation values. On the other hand, variation of both delivery pressure and angular velocity does not seem to produce evident effects on this parameter.

Results obtained from the experimental campaign demonstrate that radial clearances measured at the end of the production process may show high value of the estimated standard deviation, even if the recorded values stand within the design tolerance interval. Moreover, although design limitations are satisfied, slight modifications of the radial clearances may consistently affect the pump performance, both in terms of volumetric efficiency and required torque. In addition, such a phenomenon is clearly amplified as the temperature increases.

3.8 MODEL RESULTS AND VALIDATION

In the present Section, results obtained from the numerical model described in Sections from 3.2 to 3.6 are introduced and discussed. Attention is particularly focused on the comparison with data obtained from the experimental campaign described in Section 3.7, with the aim to precisely address the accuracy of the model. All the data reported in this Section refer to the reference system defined in Figure 42. As enlightened in the previous Section, the experimental data suggest that a proper validation of the model should refer to the actual geometry of the tested sample. If the comparison between numerical and measured data is performed by using a single pump sample, the set up of the model should be based on the actual geometrical parameters of that sample, and not on the design values. Concurrently, a similar approach

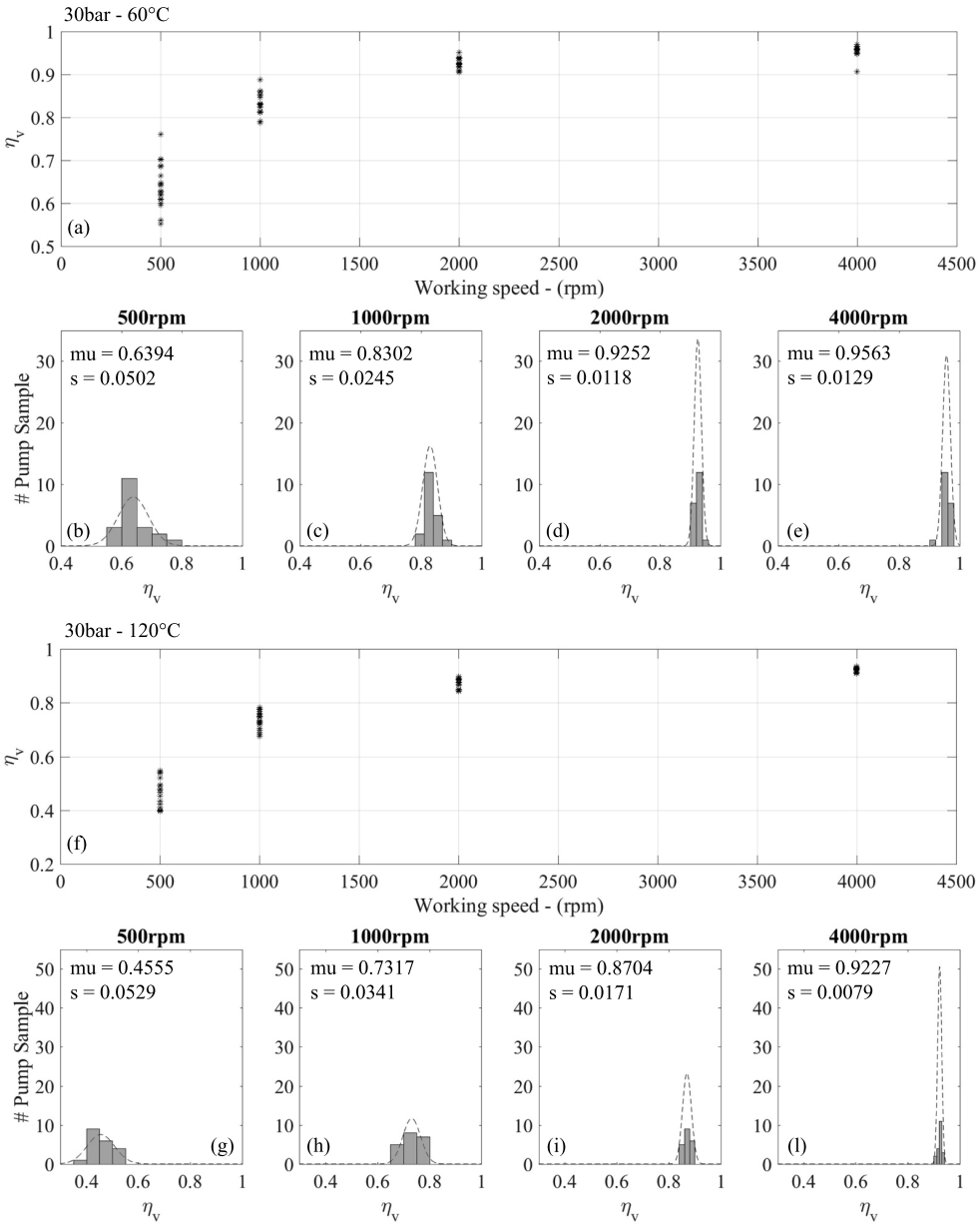

Figure 39: Measured efficiency η_v with respect to speed variation, for the 20 samples. From (a) to (e), test conditions are: $P_{out} = 30bar$ and $T_{oil} = 60°C$, while from (f) to (l) refer to the same case with $T_{oil} = 120°C$. Data are normally distributed for each analyzed working condition.

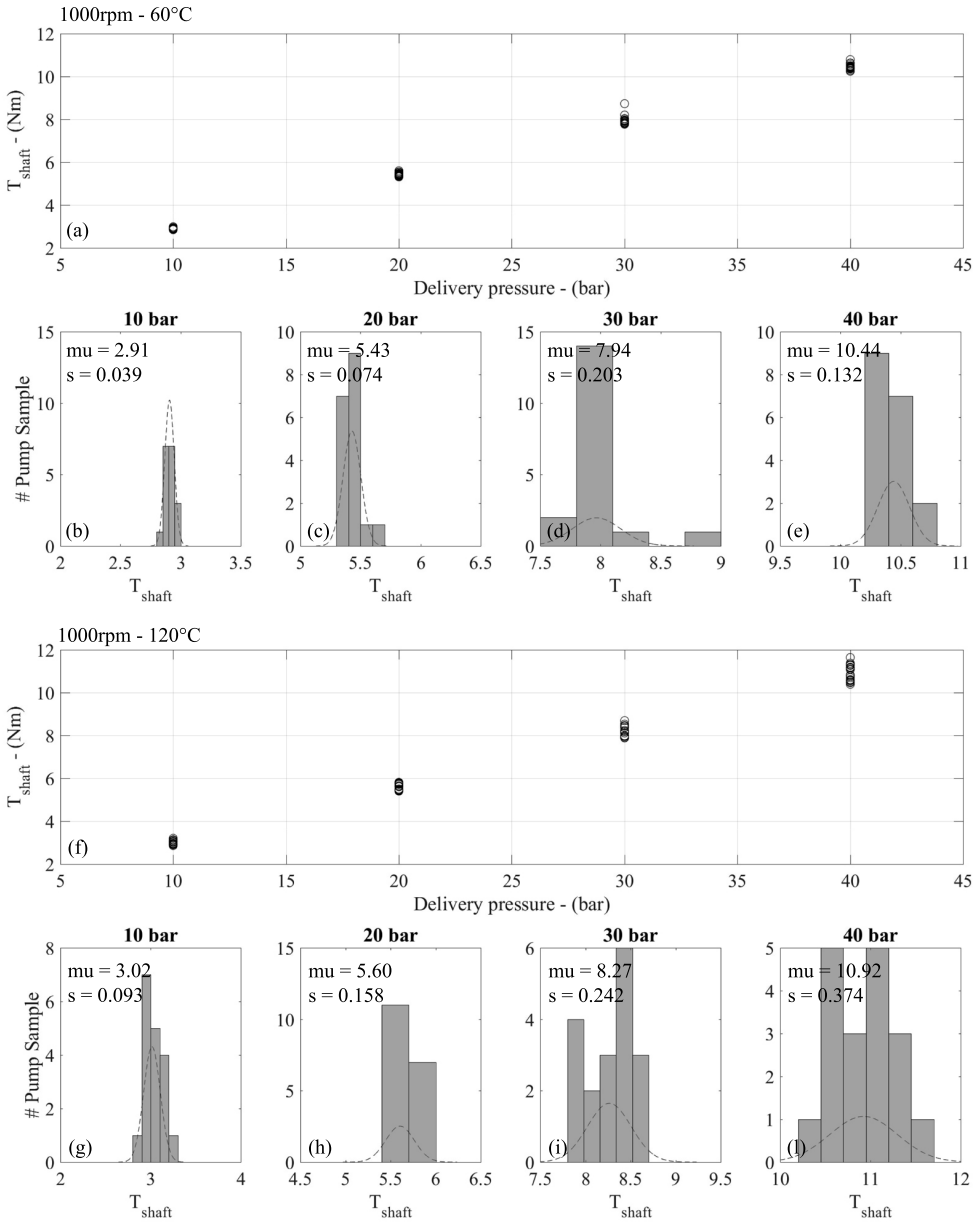

Figure 40: Torque T_{shaft} required to operate the pump with respect to pressure variation, for the 20 samples. From (a) to (e), test conditions are: $n = 1000rpm$ and $T_{oil} = 60°C$, while from (f) to (l) test conditions are: $n = 1000rpm$ and $T_{oil} = 120°C$. Data are normally distributed for each analyzed working condition.